Power Electronic Systems
Laboratory

Proceedings of the 25th International Conference on Electrical Machines and Systems (ICEMS 2022), Chiang Mai, Thailand, November 29-December 2, 2022

Eddy Current Linear-Rotary Position Sensor for an Implantable Total Artificial Heart

R. Giuffrida,
J. W. Kolar,
D. Bortis

Eidgenössische Technische Hochschule Zürich
Swiss Federal Institute of Technology Zurich

Eddy-Current Linear-Rotary Position Sensor for an Implantable Total Artificial Heart

Rosario V. Giuffrida, Johann W. Kolar and Dominik Bortis
Power Electronic Systems Laboratory, ETH Zurich, Zurich, Switzerland
giuffrida@lem.ee.ethz.ch

***Abstract*—This paper presents an eddy-current linear-rotary position sensor for *ShuttlePump*, an implantable total artificial heart based on a linear-rotary actuator. The sensor is obtained by extending a commercially available rotary position sensor with appropriate data processing by also capturing the information about the linear position. In fact, with changing linear distance of the target, the amplitudes of the sine and cosine sensor outputs change. Furthermore, the commercial IC serving as interface for the rotary sensor adjusts its excitation frequency due to the changing coupling between the sensor and the linearly moving target. Hence, there are two options to additionally measure the linear position, which are analyzed theoretically with finite element simulations, validated experimentally and compared in terms of achievable sensitivity, bandwidth and linearity. Both options allow to reach z-resolutions below the required 100 µm and a φ-accuracy in the 5° range while meeting the specified 100 Hz bandwidth requirement and can hence be used for feedback position control of *ShuttlePump*.**

I. Introduction

Contactless position measurement of a moving target following a linear and/or rotary motion is essential to ensure the correct operation of many actuators in different applications [1]–[5]. Among contactless position sensors, magnetic sensors (such as e.g. Hall-effect or magneto-resistive sensors) or Eddy Current Sensors (ECSs) are the preferred choice and offer position resolutions even down to the nm range [6]. In the case of Linear-Rotary Actuators (LiRAs), it is necessary to measure accurately both linear and rotary positions of the *mover*, i.e. the movable part carrying/serving as the end-effector. The simplest approach is to use two sensors to capture linear and rotary motion independently. However, for applications that require a high level of integration, a combined solution is needed. This is the case for *ShuttlePump* (cf. **Fig. 1 (a)**), a novel implantable total artificial heart currently under development at the Power Electronic Systems Laboratory, ETH Zurich in partnership with *Charité Berlin* and the *Medical University of Vienna* [7]. *ShuttlePump* is a valveless pulsatile blood pump based on a LiRA. Its specially-shaped piston is enclosed in a cylindrical housing and divides it into two chambers serving as left and right heart ventricles. With its linear-rotary motion, the piston of *ShuttlePump* is responsible for opening/closing the pump's inlets and outlets while being linearly actuated to pump blood in the systemic/pulmonary circulations (cf. **Fig. 1 (b)**). Furthermore, the piston is continuously rotating immersed in blood, thus supporting itself radially with a journal hydrodynamic bearing that prevents any contact with the housing. In order to ensure the correct operation of *ShuttlePump*, the linear and rotary positions of its piston have to be measured and controlled accurately. On one hand, this guarantees that the opening/closing times of the inlets/outlets are respected tightly, in order to avoid dangerous pressure peaks and prevent the piston from touching the housing axially. On the other hand, this information is needed to implement a field-oriented control scheme for the *ShuttlePump*'s LiRA, realized as a PMSM, thus generating the highest

978-1-6654-9302-4/22/$31.00

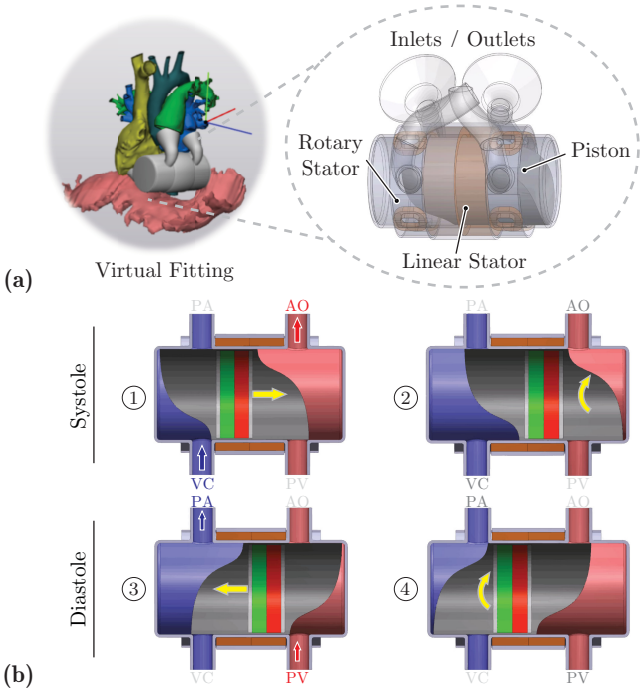

Fig. 1: (a) The implantable total artificial heart *ShuttlePump*, based on a linear-rotary moving piston. Most of the enclosure's lateral surface is occupied by the stators of the LiRA, hence the position sensors have to be placed on the axial surfaces. **(b)** Cut views showing the operating principle of *ShuttlePump*. With its linear motion (stages 1 and 3), the piston pushes the blood into the Aorta (AO) or the Pulmonary Artery (PA) for the systemic and pulmonary circulation, respectively. With the rotary motion (stages 2 and 4), opening/closing of the pump's inlets/outlets is controlled. Both motions are executed simultaneously with an operational frequency of $f_{\mathrm{op}} = 5\,\mathrm{Hz}$.

force/torque output with the least ohmic losses. For these reasons, the required linear and rotary position measurement resolutions are in the range of 100-250 µm and 1-5°, with a targeted bandwidth of at least 50 Hz (i.e. 10 times larger than the operational motion frequency $f_{\mathrm{op}} = 5\,\mathrm{Hz}$). All the specifications of the application are also reported in **Tab. I**. Another challenge in the design of the sensor is the very limited accessibility of the piston surface, since the lateral surface of the pump is largely occupied by the stators of the LiRA. Therefore, there is no space inside the stator for the linear and rotary position sensors, which have to be placed at the two axial ends of the housing. As a consequence, the main challenge is represented by the large air gap δ between the sensor plane and the measurement target, which increases up to $\delta_{\max} = 16\,\mathrm{mm}$ during the linear motion of the

TABLE I: Application specifications for *ShuttlePump*.

	Linear Position (z)	Rotary Position (φ)
Measurement Range	0 ... 16 mm	0 ... 360 °
Measurement Resolution	100-250 µm	1-5 °
Measurement Bandwidth	50-100 Hz	50-100 Hz

piston. This condition makes e.g. Hall sensors not suitable for this application, as the magnetic field coming from a permanent magnet target would be very weak and easily disturbed by external magnetic fields. On the other hand, ECSs are still an option, as they offer better immunity to external noise and there exist off-the-shelf solutions that can be used to measure absolute linear or rotary position [8], [9]. However, due to the tight space constraints of *ShuttlePump*, it is desirable to use only one ECS to capture both motions. Hence, this paper discusses the design and realization of a highly-integrated eddy-current-based linear-rotary position sensor for *ShuttlePump*, obtained by extending a commercial "single-axis" ECS with additional data processing. In **Sec. II**, the general operating principle of the sensor is explained and the proposed sensor concept is presented. **Sec. III** discusses two data processing options to extend a commercial rotary ECS into a full linear-rotary position sensor and compares them in terms of sensitivity, achievable resolution and bandwidth. In **Sec. IV**, the design and realization of the PCB-embedded sensor prototype are presented. **Sec. V** verifies with experimental measurements the proposed linear-rotary sensor and discusses the results evaluating the sensitivities obtained with both concepts. Finally, **Sec. VI** concludes the paper.

II. Sensor's Operating Principle

An ECS exploits the variation of magnetic coupling existing between an excitation coil carrying a high frequency current and the secondary magnetic field generated by the induced eddy currents circulating in a nearby conductive target. As depicted in **Fig. 2**, the excitation coil is usually placed with its axis perpendicular to the target, such that the maximum amount of primary magnetic flux is linked by it, and therefore larger eddy currents are induced. Typically, an ECS measures variations of the air gap length $\delta(t)$ between the excitation coil and the target, as this directly affects the amount of total magnetic flux that is linked by one turn of the excitation coil, i.e.

$$\Phi_{\mathrm{exc}}(\delta,t) = \iint_{\mathcal{S}} B(\delta,t)\,\mathrm{d}S, \tag{1}$$

where $B(\delta,t)$ is the flux density and $\mathcal{S}$ the excitation coil's (integration) area. As a result, the equivalent input impedance of the excitation coil $Z_{\mathrm{in,exc}}(\delta,t)$ varies and it can be used to measure $\delta(t)$. As an alternative, the total magnetic flux can also be linked by a separate pick-up coil placed nearby, at whose terminals an induced voltage $u_{\mathrm{pick}}(t)$ appears, according to Faraday's law of induction

$$u_{\mathrm{pick}}(\delta,t) = -N_{\mathrm{pick}}\frac{\mathrm{d}\Phi_{\mathrm{pick}}(\delta,t)}{\mathrm{d}t}, \quad \Phi_{\mathrm{pick}}(\delta,t) = \iint_{\mathcal{P}} B(\delta,t)\,\mathrm{d}P, \tag{2}$$

where N_{pick} is the number of turns of the pick-up coil (here assumed to be all identical), $\Phi_{\mathrm{pick}}(\delta,t)$ the magnetic flux of the pick-up coil and $\mathcal{P}$ its (integration) area.

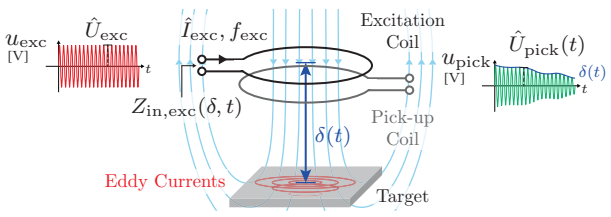

Fig. 2: Basic operating principle of a conventional ECS, consisting of an excitation coil, a conductive target and (eventually) a pick-up coil. The variable air gap length $\delta(t)$ can be measured either from the excitation coil's equivalent input impedance $Z_{\mathrm{in,exc}}(\delta,t)$ or from the induced voltage $u_{\mathrm{pick}}(\delta,t)$ in the pick-up coil.

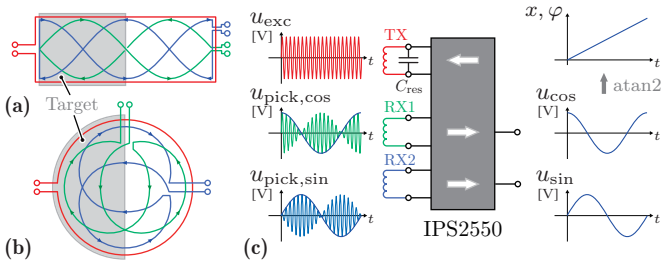

Fig. 3: Inductive position sensor from *Renesas*, a fixed-air-gap-length variable-coil-shape ECS with excitation coil (red) and two 90° spatially displaced pick-up coils (green and blue) to uniquely determine the target position. **(a)** Linear position sensor realization and **(b)** rotary position sensor realization. **(c)** Integrated sensor interface *IPS2550* with a transmitter and two receivers with coherent demodulators, providing either the linear position (x) or rotary position (φ) of the target.

Consequently, as it can be noticed from (1) and (2), the total magnetic flux of the excitation or pick-up coils also depends on their coil area, $\mathcal{S}$ or $\mathcal{P}$. This offers another realization option for the ECS, namely if the coils are shaped in a special way with respect to the target, e.g. along a certain direction $x(t)$, it is possible to obtain a variable $Z_{\mathrm{in,exc}}(x,t)$ or $u_{\mathrm{pick}}(x,t)$ even with a fixed air gap length δ. An example of this realization is the inductive position sensor proposed and commercially available by *Renesas* [9]–[11] as shown in **Fig. 3**. This ECS can be designed to measure either linear (cf. **Fig. 3 (a)**) or rotary (cf. **Fig. 3 (b)**) positions by utilizing special sinusoidally-shaped pick-up coils that can be conveniently realized on a PCB. In particular, the induced voltage u_{pick} appearing at the terminals of the pick-up coil is sinusoidally modulated in amplitude by the position of the target along the linear x or rotary φ direction. In order to gain unique position information, 90° spatially displaced coils are used to obtain sine- and cosine-modulated signals $u_{\mathrm{pick,sin}}$ and $u_{\mathrm{pick,cos}}$, which can be used after demodulation to calculate x or φ as the argument $\{x,\varphi\}(t) = \mathrm{atan2}(u_{\sin}, u_{\cos})$ as typically done for e.g. a resolver. As for conventional ECS, a sensor interface is needed in order to drive the excitation coil and demodulate plus eventually post-process the measurement signal(s). For this purpose fully-integrated solutions exist, like the *Renesas IPS2550* [9], which specifically offers two demodulation channels for the discussed inductive position sensor (cf. **Fig. 3 (c)**). For such ECS realization with variable-shape pick-up coils, an air gap variation is typically a problem, because if the amplitude of $u_{\mathrm{pick,sin}}$ and $u_{\mathrm{pick,cos}}$ reduces, the achievable resolution of φ, calculated from $u_{\sin}$ and $u_{\cos}$ after sampling and quantization with an ADC, is also worsened. In order to prevent this, the effect of a variable air gap can be eliminated/compensated with appropriate post-processing or,

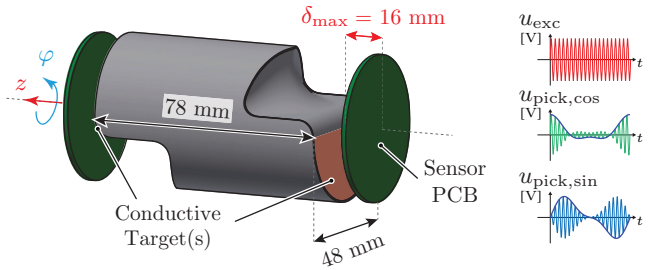

Fig. 4: The piston of *ShuttlePump* with a thin 0.5 mm highly conductive target (made of e.g. copper) embedded below its outer axial surface. The multi-layer-PCB-embedded linear-rotary ECS prototype, described in detail in **Sec. IV**, is placed right in front. A second identical sensor and target can be placed at the opposite axial surface to realize a differential sensor.

as e.g. in the case of the *IPS2550*, with an automatic adjustment of the receivers' amplifiers gain (Automatic Gain Control, AGC) [9]. Nevertheless, this issue can be turned into a feature when it comes to a full linear-rotary ECS realization, since along the axial direction this configuration still corresponds to the variable air gap length type ECS of **Fig. 2**. Therefore, instead of compensating the air gap length variations, it is possible to use them to measure the linear position $z(t)$. The proposed sensor concept consists then of a variable-coil-shape rotary ECS as the one of **Fig. 3 (b)**, extended to a full linear-rotary position sensor by also measuring the variable air gap length with appropriate data processing. As illustrated in **Fig. 4**, the semi-circular conductive target is embedded in both piston's axial surfaces and one sensor PCB per side is used in a *differential sensor configuration*. This way, it is necessary to measure with high sensitivity only till half the distance, i.e. $8\,\mathrm{mm}$ instead of $16\,\mathrm{mm}$. This allows accurate position control each time the piston is closest to either ECS, in order to avoid any collision with the enclosure along the axial direction.

III. Extension to a Linear-Rotary Sensor

In order to extend the commercial rotary ECS from *Renesas* into a full linear-rotary ECS, it is necessary to extract information about the mover's axial position $z(t)$. This can be done in two possible ways, discussed in the following.

A. Option 1: Magnitude and Argument

As mentioned, for a fixed air gap length the demodulated voltages $u_{\sin}$ and $u_{\cos}$ are used to calculate the rotary position $\varphi(t)$. If the air gap length $\delta(t)$ (from now on equivalent to the linear position $z(t)$) is varied, the magnetic coupling and hence the mutual inductance between the eddy currents' circulation paths in the target and the pick-up coil(s) changes. As a result, the amplitude of both induced voltages changes. This can be easily calculated from the magnitude of the two demodulated signals as

$$u_{\mathrm{mag}} = \sqrt{u_{\sin}^2 + u_{\cos}^2}, \tag{3}$$

which is known to be independent from $\varphi(t)$ and therefore is a good option to obtain $z(t)$. In the specific case of the *Renesas IPS2550*, this is actually the calculation used in the IC to correct air gap variations with the AGC [9]. Consequently, in order to also measure the linear distance by means of the amplitude variation, the ACG must be disabled and the IC must be operated with constant gain. The main drawback of this option lies in the noticeable sensitivity degradation for increasing linear position z, which also leads to reduced angle resolution, especially without AGC. This is because the magnetic coupling between the excitation coil and the target decreases exponentially with increasing distance, a well-known fact in ECS design [12]. The dependence of the voltage amplitude on the distance can be verified by a simple 3D FEM simulation (cf. **Fig. 5**), where the amplitude of the induced voltage in the pick-up coil is recorded for increasing values of z from $0\,\mathrm{mm}$ to $8\,\mathrm{mm}$. The simulation is performed for the reference case with $\hat{I}_{\mathrm{exc,ref}} = 1\,\mathrm{A turns}$ and $f_{\mathrm{exc,ref}} = 5\,\mathrm{MHz}$. In order to obtain realistic results, it should be observed that the *IPS2550* can drive the excitation coil only in resonance with a parallel capacitor C_{res} (cf. **Fig. 5 (a)**). Moreover, remember that although not used for measurement, the equivalent input impedance of the excitation coil $Z_{\mathrm{in,exc}}$ still changes with z. Specifically, if the inductance $L_{\mathrm{in,exc}}(z)$ varies, the *IPS2550* adjusts its excitation frequency f_{exc} to the resonance frequency $f_{\mathrm{res}}(z) = \frac{1}{2\pi\sqrt{L_{\mathrm{in,exc}}(z)C_{\mathrm{res}}}}$. In **Fig. 5 (b)**, the simulated $L_{\mathrm{in,exc}}(z)$ is shown and used to calculate the corresponding $f_{\mathrm{res}}(z)$. As a reference case, the value of C_{res} is selected such that $f_{\mathrm{res}}(z = 0\,\mathrm{mm}) = f_{\mathrm{exc,ref}} = 5\,\mathrm{MHz}$. Another consequence of the variable $f_{\mathrm{res}}(z)$ is that also the amplitude of the current $\hat{I}_{\mathrm{exc}}(z)$ resonating between C_{res} and the excitation coil depends on z and has to be considered. For a fixed unity driving voltage $\hat{U}_{\mathrm{exc}} = 1\,\mathrm{V}$, this is obtained as $\hat{I}_{\mathrm{exc}}(z) = \hat{U}_{\mathrm{exc}}\,\omega_{\mathrm{res}}(z)\,C_{\mathrm{res}}$, with $\omega_{\mathrm{res}}(z) = 2\pi f_{\mathrm{res}}(z)$. The simulated B field distribution, an example of which is shown in **Fig. 5 (c)**, is integrated in the pick-up coil area to obtain the amplitude of the flux $\hat{\Phi}_{\mathrm{pick}}(\varphi, z)$ for each value of z and φ. Finally, the amplitude of the induced voltage is

$$\hat{U}_{\mathrm{pick}}(\varphi, z) = -N_{\mathrm{pick}}\,\omega_{\mathrm{res}}(z)\,\hat{\Phi}_{\mathrm{pick}}(\varphi, z)\left(\frac{\hat{I}_{\mathrm{exc}}(z)}{\hat{I}_{\mathrm{exc,ref}}}\right). \tag{4}$$

For the given coil dimensions, induced peak voltages of about $12\,\mathrm{mV}$ per turn can be expected for the reference case, as shown in **Fig. 5 (d)** and **Fig. 5 (e)**, where the simulated pick-up voltage is given as a function of rotary and linear position, respectively. Over an axial distance of $8\,\mathrm{mm}$, $u_{\mathrm{pick,mag}}$ reduces by about 85% and hence the z-sensitivity decreases significantly. In order to limit this effect, $\hat{U}_{\mathrm{pick}}(\varphi, z)$ should be maximized with three possible options. As it appears from (4), one option is to maximize the excitation frequency f_{exc}, which for the *IPS2550* is limited to $5.6\,\mathrm{MHz}$. In practice, though, there is also an upper limit due to the unavoidable parasitic capacitance C_{p} that results in practical coil realizations. In fact, this leads to a certain Self-Resonant-Frequency (SRF) $f_{\mathrm{SRF}} = \frac{1}{2\pi\sqrt{L_{\mathrm{pick}}C_{\mathrm{p}}}}$ of the pick-up coil, above which it exhibits predominantly a capacitive behavior. As a rule of thumb, it is advisable to select $f_{\mathrm{exc}} \ll f_{\mathrm{SRF}}$, separating the two by e.g. a factor 5 to 10. The second option appearing from (4) is

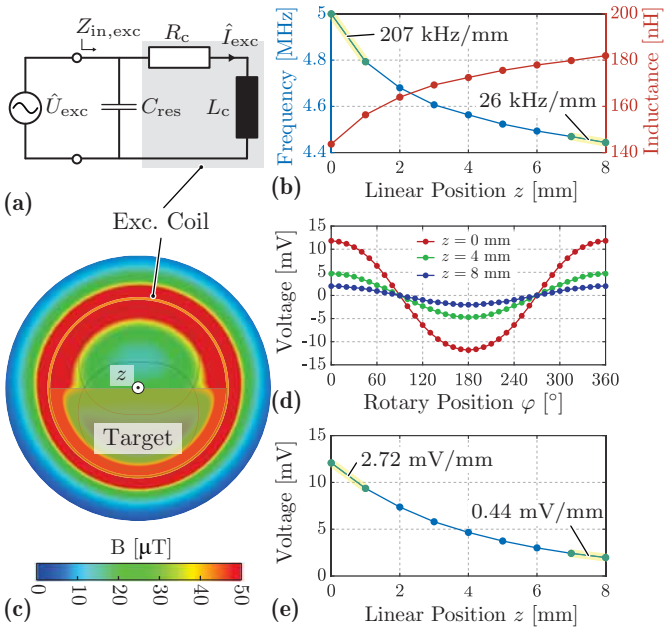

Fig. 5: 3D FEM simulation results (*ANSYS Maxwell*) to verify the magnitude-based measurement *Option 1*. **(a)** Driving stage of the *Renesas IPS2550*, i.e. an oscillator with parallel resonance. **(b)** Simulated excitation coil inductance profile $L_{\mathrm{in,exc}}(z)$, from which the resonant frequency $f_{\mathrm{res}}(z)$ is calculated with a reference capacitor $C_{\mathrm{res}} = 7.05\,\mathrm{nF}$. The best- and worst-case frequency sensitivities are indicated. **(c)** Simulated distribution of the B field for $z = 1\,\mathrm{mm}$ with $f_{\mathrm{exc,ref}} = 5\,\mathrm{MHz}$ and $\hat{I}_{\mathrm{exc,ref}} = 1\,\mathrm{A turns}$. **(d)** Amplitude $\hat{U}_{\mathrm{pick}}(\varphi, z)$ of the induced voltage in one of the pick-up coils $u_{\mathrm{pick}(,\cos)}(\varphi, z) = \hat{U}_{\mathrm{pick}}(\varphi, z)\,\sin(2\pi f_{\mathrm{exc}}\,t)$ for $z = \{0, 4, 8\}\mathrm{mm}$. **(e)** Magnitude from the demodulated $u_{\sin}$ and $u_{\cos}$ versus the linear position z, with indicated best- and worst-case amplitude sensitivities.

to increase the number of turns of the pick-up coil N_{pick}. As shown in **Sec. IV**, special care must be taken in the design, as multiple turns also increase the parasitic capacitance C_{p} (e.g. if multiple PCB layers are used), with the result that f_{SRF} is decreased. Finally, the (fixed) internal gain of the IC receivers can be maximized. The *IPS2550* has a maximum output voltage swing of 3 Vpp for 5 V operation, so the internal gain is programmed in such a way that at $z = 0\,\text{mm}$ this swing is achieved. This way, the z-sensitivity becomes $338\,\text{mV/mm}$ at $z = 0\,\text{mm}$ and $54.8\,\text{mV/mm}$ at $z = 8\,\text{mm}$. The final z-resolution is defined by the number of bits of the ADC used to sample $u_{\sin}$ and $u_{\cos}$: 10 bits, for example, allow to resolve $5\,\text{V}/2^{10} = 4.8\,\text{mV}$, corresponding to $14.5\,\mu\text{m}$ at $z = 0\,\text{mm}$ and to $89\,\mu\text{m}$ at $z = 8\,\text{mm}$.

B. Option 2: Frequency and Argument

A second way to measure the linear position z is deduced from the frequency variation shown in **Fig. 5 (b)**, where it can be observed that the excitation frequency f_{exc} selected by the *IPS2550* depends on the linear position z, since the self-inductance is changing with the axial distance of the target and the IC always tracks the LC resonance frequency. According to the FEM simulation, a maximum sensitivity of $207\,\text{kHz/mm}$ at $z = 0\,\text{mm}$, reducing to $26\,\text{kHz/mm}$ at $z = 8\,\text{mm}$ is to be expected. There are two main advantages when utilizing f_{exc} to measure z. The first one is that the *IPS2550* can be operated with the AGC enabled and in this way the demodulated $u_{\sin}$ and $u_{\cos}$ retain a constant amplitude even for increased distances z. As a consequence, the measurement accuracy of the calculated φ is improved and decoupled from z. The second one is that the z measurement resolution can be increased by trading-off measurement bandwidth. This is because the resolution of frequency counters implemented digitally on an MCU depends directly on the duration of the counting time interval [13]. If f_{count} is the counter's frequency, $f_{\text{signal}} = f_{\text{exc}}$ the frequency to be measured and P the number of counted periods of f_{signal}, it can be shown that the frequency resolution is

$$\Delta f \approx \frac{f_{\text{signal}}^2}{f_{\text{count}}} \frac{1}{P} \tag{5}$$

i.e. it can be enhanced by acquiring multiple periods P of f_{signal}. Clearly, this reduces the measurement bandwidth since it increases the latency, as a measurement is complete only when and shortly after the counter is stopped. The measurement bandwidth is then approximately

$$f_{\text{BW}} \approx f_{\text{signal}} \frac{1}{P}. \tag{6}$$

For a measurement bandwidth of e.g. 100 Hz and $f_{\text{signal}} = f_{\text{exc}} = 5\,\text{MHz}$, it results $P = 50000$. Therefore, with a MCU clock frequency of $f_{\text{count}} = 100\,\text{MHz}$, the frequency resolution is $\Delta f = 5\,\text{Hz}$ at $z = 0\,\text{mm}$ and $\Delta f = 3.94\,\text{Hz}$ at $z = 8\,\text{mm}$. This corresponds to a z-resolution of $24.2\,\text{nm}$ and $151.9\,\text{nm}$, respectively. A schematic representation of the chosen hardware implementation for this frequency-based measurement option is shown in **Fig. 6**.

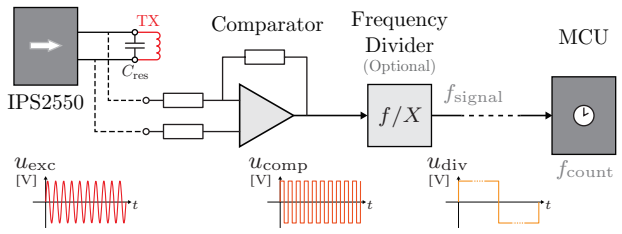

Fig. 6: Schematic of the frequency-based measurement *Option 2*. The high frequency excitation signal u_{exc} is converted into a square wave signal u_{comp} with a high-speed comparator for further logic counting with an MCU, running with clock frequency f_{count}. In case the distance between comparator and MCU is not negligible, a frequency divider stage can be optionally included to mitigate electromagnetic noise emissions.

IV. Hardware Prototype

The presented linear-rotary ECS is realized as an integrated PCB hardware prototype, shown in **Fig. 7 (b)**. It consists of a *sensor head* (excitation and pick-up coils) and a *sensor interface* for demodulation and frequency detection.

A. Measurement Requirements

The sensor is realized taking into account the measurement requirements defined by the application, i.e. by *ShuttlePump*'s geometry and operation. During the linear motion, it is possible that the piston tilts, as the hydrodynamic bearing supporting it is realized with a $140\,\mu\text{m}$ gap. Given the piston's dimensions, this leads to a maximum error of $2 \cdot 90\,\mu\text{m}$ in the linear position z. It is therefore not reasonable to target a z-accuracy below $200\,\mu\text{m}$. Nevertheless, another important requirement is that the piston does not collide with the enclosure when maximally displaced to one side. The z-accuracy must hence be below e.g. $0.5\,\text{mm}$. Finally, opening and closing of the inlets/outlets imposes a requirement on the maximum φ measurement error. Considering that the piston's shape allows for a maximum error of 2 mm along the circumferential direction, with the piston's diameter of $48\,\text{mm}$ a φ measurement error no larger than $5°$ can be allowed.

B. PCB-embedded Realization

The outer diameter of the PCB prototype is maximized to $48\,\text{mm}$, chosen according to *ShuttlePump*'s geometry, i.e. of its piston and enclosure. The circular excitation coil has a diameter of $46.8\,\text{mm}$ and covers the largest possible area with the primary magnetic field. The sine- and cosine-shaped pick-up coils cover most of the PCB area between the inner and outer diameters of $17\,\text{mm}$ and $42.4\,\text{mm}$, respectively. The inner radius is chosen such that enough space is left to place the *Renesas IPS2550* sensor interface. The PCB is realized

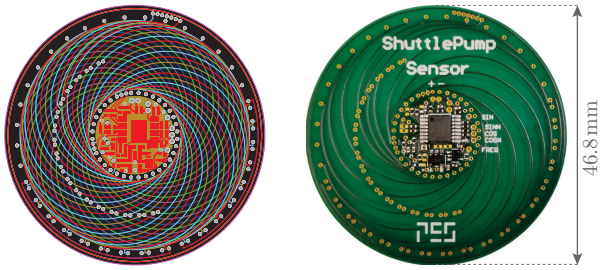

Fig. 7: Multi-layer-PCB-embedded linear-rotary ECS. **(a)** Layout details (*Altium Designer*) with distributed shifted turns and **(b)** realized hardware prototype.

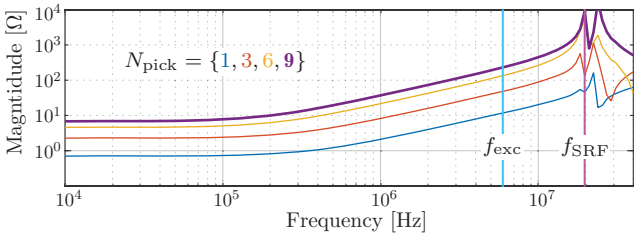

Fig. 8: Impedance magnitude of one of the pick-up coils, measured on the realized prototype for different number of turns N_{pick}. Due to the distributed layout with shifted turns, it can be verified that f_{SRF} remains around 20 MHz and a high $f_{\text{exc}} = 5\,\text{MHz}$ can be safely selected.

with 6 layers that are all spanned by both the excitation and pick-up coils. Therefore, the number of turns of the excitation coil is $N_{\mathrm{exc}} = 6$. For the pick-up coils, the number of turns is instead $N_{\mathrm{pick}} = 9$ and can only be reached with the special PCB layout shown in **Fig. 7 (a)**. As it can be noticed, the coil is distributed in multiple layers and each turn is shifted along the φ-direction with respect to the previous one. Although this way more turns can be fit in less layers, it should be noticed that the *effective* number of turns $N_{\mathrm{pick,eff}}$ is lower than N, as each turn links more or less magnetic flux according to the relative position to the target. Another advantage of shifting the turns is that the total parasitic capacitance C_{p} is smaller with respect to the case of perfectly overlapped turns, thus allowing to select f_{exc} as high as possible. In **Fig. 8**, showing the measured impedance magnitude of one of the realized pick-up coils, it can be observed that f_{SRF} stays around 20 MHz even with $N_{\mathrm{pick}} = 9$. Consequently, to maximize the induced voltage in the pick-up coils $f_{\mathrm{exc}} = f_{\mathrm{SRF}}/4 = 5\,\mathrm{MHz}$ can be selected, which is close to the maximum possible excitation frequency that the *IPS2550* can provide. Finally, in order to implement *Option 2*, a comparator is included, which generates the digital signal u_{comp} used for frequency detection. In addition, since the MCU unit of *ShuttlePump* is placed outside the body and the signals have to be transmitted via a percutaneous drive line of $\approx 1\,\mathrm{m}$ length, a flip-flop-based frequency divider with $X = 1024$ stages is included to decrease the sensor frequency without degrading the sensitivity.

V. Measurements and Results

In order to verify the sensor's functionality, the realized PCB-embedded prototype is mounted on the custom test bench shown in **Fig. 9**. The target thickness should be selected larger than the skin depth, which is 30 µm for copper at $f_{\mathrm{exc}} = 5\,\mathrm{MHz}$. Due to mechanical stability, 3 mm is chosen. The test bench features two precision linear and rotary positioning stages, which allow to accurately adjust the target's linear and rotary positions down to the µm range and fractions of °.

A. Option 1: Magnitude and Argument

For *Option 1*, the AGC of the *IPS2550* is disabled, such that the magnitude variations of the received signals are not compensated. The measurements are reported in **Fig. 10 (a.i, b.i, c.i)**. For each value of the linear position $z = \{0, 4, 8\}\mathrm{mm}$, the rotary position is increased in steps of 10° from 0° to 360°. Even though the amplitude of the induced voltages noticeably reduces for increasing z, the demodulated voltages of **Fig. 10 (a.i)** can still be used to calculate φ pretty accurately. The argument shown in **Fig. 10 (b.i)** is calculated

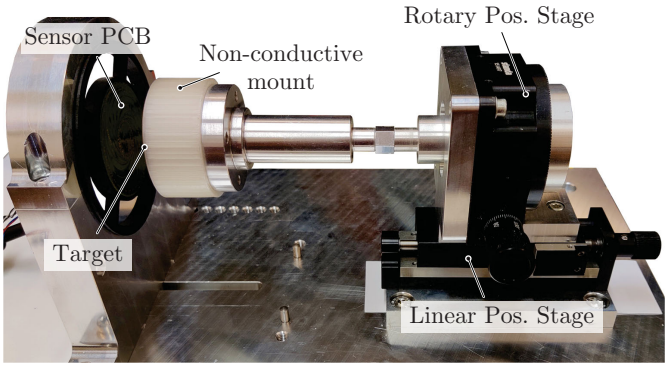

Fig. 9: Test bench used for the experimental sensor characterization. The sensor PCB is fixed to the base plate and the semi-circular conductive target is mounted on a non-conductive support. The target's position can be accurately adjusted with a linear and a rotary stage.

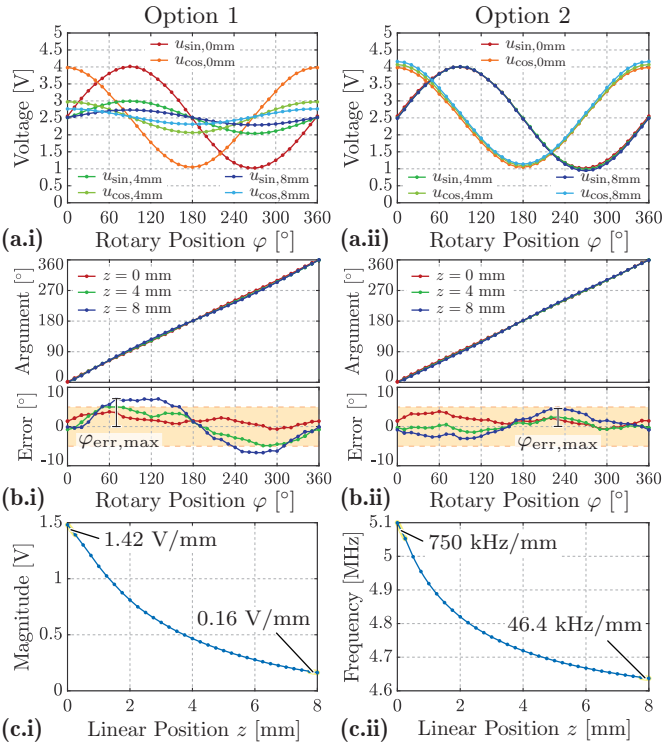

Fig. 10: Experimental measurements for the linear-rotary ECS for both z measurement options. **(a.i, a.ii)** Measured voltages u_{sin} and u_{cos} at the output of the *IPS2550* without (*Option 1*) or with (*Option 2*) AGC for $z = \{0, 4, 8\}\mathrm{mm}$. **(b.i, b.ii)** Calculated argument from u_{sin} and u_{cos} and resulting φ measurement error for $z = \{0, 4, 8\}\mathrm{mm}$. **(c.i)** Measured magnitude of u_{sin} and u_{cos} versus the linear position z, with indicated best- and worst-case amplitude sensitivities. **(c.ii)** Measured excitation frequency f_{exc} versus the linear position z, with indicated best- and worst-case frequency sensitivities.

TABLE II: Linear-Rotary ECS measurement results.

	Option 1	*Option 2*
z-sensitivity	1.42 - 0.16 V/mm	750 - 46.4 kHz/mm
z-resolution	3.39 - 30 µm	6.75 - 90.5 nm
z-bandwidth	10 kHz	100 Hz
φ-error (max)	3.75 - 7 °	3.84 - 4.58 °
φ-bandwidth	10 kHz	10 kHz

taking into account that the measured u_{sin} and u_{cos} are sampled with a 10-bits ADC and are hence quantized in 1024 levels. This influences the final φ-error, which is shown right below the calculated argument. The worst case occurs for the greatest distance $z = 8\,\mathrm{mm}$, as u_{sin} and u_{cos} have the smallest amplitude then and hence their quantization is more coarse. As a result, the maximum φ-error is $\varphi_{\mathrm{err,max}} = 7°$, which results in a worst-case percentage non-linearity of 1.94%. For what concerns the linear position z, from the results of **Fig. 10 (c.i)** it is possible to calculate the best- and worst-case z-sensitivities, which are $1.42\,\mathrm{V/mm}$ at $z = 0\,\mathrm{mm}$ and $0.16\,\mathrm{V/mm}$ at $z = 8\,\mathrm{mm}$, respectively. Consequently, with a 10-bits ADC, the final z-resolution is 3.39 µm at $z = 0\,\mathrm{mm}$ and 30 µm at $z = 8\,\mathrm{mm}$. Finally, the measurement bandwidth for both z and φ is in this case defined by the cutoff frequency of the internal low-pass filter used for demodulation, which for the *IPS2550* is 10 kHz [9]. An alternative worth mentioning for *Option 1*, although not implemented, would be to keep the AGC enabled and read periodically the internal gain used by the AGC via the I2C interface used to program the IC. This allows to obtain magnitude information while retaining the full amplitude for u_{sin} and u_{cos}.

B. Option 2: Frequency and Argument

For *Option 2*, the AGC of the *IPS2550* is enabled instead, as the linear position is measured from the excitation frequency f_{exc}. The measurements are then repeated and shown in **Fig. 10 (a.ii, b.ii, c.ii)**. Due to the AGC, the amplitude of the induced voltages in **Fig. 10 (a.ii)** does not reduce for increasing z. Therefore, $u_{\sin}$ and $u_{\cos}$ are always quantized into the same number of levels, which with the argument calculation of **Fig. 10 (b.ii)** translates into a lower φ-error for the worst-case of $z = 8\,\mathrm{mm}$. This time, in fact, the maximum error is $\varphi_{\mathrm{err,max}} = 4.58°$, which results in a percentage non-linearity of 1.27%. From the results of **Fig. 10 (c.ii)**, showing this time how f_{exc} varies versus z, the best- and worst-case z-sensitivities are $750\,\mathrm{kHz/mm}$ at $z = 0\,\mathrm{mm}$ and $46.4\,\mathrm{kHz/mm}$ at $z = 8\,\mathrm{mm}$, respectively. As discussed in **Sec. III-B**, in this case the measurement resolution is defined according to (5). The MCU clock is $f_{\mathrm{count}} = 100\,\mathrm{MHz}$ and due to the frequency divider $f_{\mathrm{signal}} = f_{\mathrm{exc}}/1024 = 4.98\,\mathrm{kHz}$ at $z = 0\,\mathrm{mm}$ and $f_{\mathrm{signal}} = f_{\mathrm{exc}}/1024 = 4.53\,\mathrm{kHz}$ at $z = 8\,\mathrm{mm}$. Consequently, for a 100 Hz measurement bandwidth $P = 50$ and $\Delta f(z = 0\,\mathrm{mm}) = 0.005\,\mathrm{Hz}$ and $\Delta f(z = 8\,\mathrm{mm}) = 0.004\,\mathrm{Hz}$, hence the achievable z-resolution is $6.75\,\mathrm{nm}$ at $z = 0\,\mathrm{mm}$ and $90.5\,\mathrm{nm}$ at $z = 8\,\mathrm{mm}$.

C. Comparison and Discussion

The achieved ECS specifications for both options are summarized in **Tab. II**. As mentioned, the effect of the AGC on the measured φ can be seen by comparing the φ-error for both cases. As it can be seen, *Option 2* benefits from it, with $\varphi_{\mathrm{err,max}}$ always below the maximum allowed 5°. Although for *Option 1* $\varphi_{\mathrm{err,max}} > 5°$ for the worst-case distance $z = 8\,\mathrm{mm}$, it should be observed that opening/closing of *ShuttlePump*'s inlets/outlets occurs when the piston is close to the enclosure's sides. In that case (i.e. $z = 0\,\mathrm{mm}$), both options are usable and offer comparable φ-accuracy with errors below 5°. For the linear position z, the frequency-based *Option 2* considerably increases the z-resolution by trading-off measurement bandwidth. Nevertheless, for the targeted application, also *Option 1* offers sufficient z-resolution. Finally, it should be mentioned that *Option 1* only requires two measurement signals ($u_{\sin}$ and $u_{\cos}$), whereas *Option 2* additionally requires the excitation voltage u_{exc} (processed into u_{div}) to measure f_{exc}.

D. Real Mission Profile - Dynamic Operation

Starting from the measurements of **Fig. 10**, it is finally possible to predict the actual sensor outputs during the dynamic operation of *ShuttlePump*. For this, the linear-rotary mission profile for one period in **Fig. 11 (a)** and **Fig. 11 (b)** is used. The linear motion follows a sinusoidal trajectory from one side of the enclosure to the other and back, while continuously rotating with constant speed, all at $f_{\mathrm{op}} = 5\,\mathrm{Hz}$. **Fig. 11 (c)** and **Fig. 11 (d)** show the resulting 2.5 V-offset-free $u_{\sin}$ and $u_{\cos}$ for *Option 1* and are generated interpolating the results of **Fig. 10 (c.i)**. The outputs are generated also for a second sensor placed on the opposite axial surface at $z = 16\,\mathrm{mm}$, thus emphasizing the advantage of using the differential measurement configuration.

VI. Conclusion

In this paper, a compact integrated eddy-current linear-rotary position sensor for *ShuttlePump* is proposed. The ECS is obtained by extending a commercial rotary ECS into a full linear-rotary one by appropriate data processing with two linear position measurement options. The experimental results show that both are usable for the targeted application, with linear and rotary position accuracies below the required $100\,\mu\mathrm{m}$ and 5° and largely sufficient measurement bandwidths $\geq 100\,\mathrm{Hz}$. Therefore, in future work, the proposed ECS can be used for feedback position control of the *ShuttlePump*'s piston.

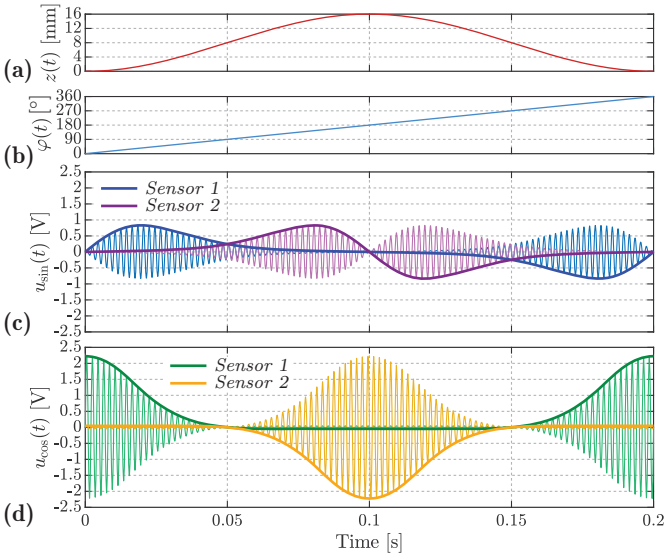

Fig. 11: Dynamic operation of *ShuttlePump* with the actual mission profiles for **(a)** linear position $z(t)$ and **(b)** rotary position $\varphi(t)$. The offset-free linear-rotary ECSs outputs for *Sensor 1* (at $z = 0\,\mathrm{mm}$) and *Sensor 2* (at $z = 16\,\mathrm{mm}$) are shown in **(c)** for the sine output $u_{\sin}$ and **(d)** for the cosine output $u_{\cos}$. The frequency of the modulation carrier is not to scale and only reported for conceptual purposes.

References

[1] S. Fericean and R. Droxler, "New Non-Contacting Inductive Analog Proximity and Inductive Linear Displacement Sensors for Industrial Automation," *IEEE Sensors Journal*, vol. 7, no. 11, pp. 1538–1545, 2007.

[2] C. Ding, J. L. G. Janssen, A. A. H. Damen, P. P. J. van den Bosch, J. J. H. Paulides, and E. Lomonova, "Modeling and Realization of a 6-DoF Contactless Electromagnetic Anti-Vibration System and Verification of its Static Behavior," in *2012 IEEE/ASME International Conference on Advanced Intelligent Mechatronics (AIM)*, pp. 149–154, 2012.

[3] A. Arcire and G. Mihalache, "Position Control of a Bidirectional Moving Magnet Actuator Based on Contactless Hall-Effect Transducer," in *2015 9th International Symposium on Advanced Topics in Electrical Engineering (ATEE)*, pp. 417–421, 2015.

[4] K. Wang, L. Zhang, S. Zheng, J. Zhou, and X. Liu, "Analysis and Experiment of Self-Differential Eddy-Current Sensor for High-Speed Magnetic Suspension Electric Machine," *IEEE Transactions on Industry Applications*, vol. 55, no. 3, pp. 2538–2547, 2019.

[5] R. Hooijschuur, N. Saikumar, S. H. HosseinNia, and R. A. J. van Ostayen, "Air-Based Contactless Wafer Precision Positioning System," *Applied Sciences*, vol. 11, no. 16, 2021.

[6] V. Chaturvedi, J. G. Vogel, K. A. A. Makinwa, and S. Nihtianov, "A 19.8-mW Eddy-Current Displacement Sensor Interface With Sub-Nanometer Resolution," *IEEE Journal of Solid-State Circuits*, vol. 53, no. 8, pp. 2273–2283, 2018.

[7] M. Granegger, T. Bierewirtz, M. Nicolai, and U. Kertzscher, "Blood Pump," EU Patent WO/2022/049166, Mar 10, 2022.

[8] Texas Instruments, "LDC Device Selection Guide," Tech. Rep. SNOA954D, Jun. 2021.

[9] Renesas Electronics Corporation, "IPS2550 Datasheet," 2022.

[10] Q. Gentjan, M. Passarotto, and R. Specogna, "Sensor Coil Optimization," US Patent 10,690,517 B2, Jun 23, 2020.

[11] A. Hoxha, M. Passarotto, G. Qama, and R. Specogna, "Design Optimization of PCB-Based Rotary-Inductive Position Sensors," *Sensors*, vol. 22, no. 13, 2022.

[12] S. D. Roach, "Designing and Building an Eddy Current Position Sensor," *Sensors - The Journal of Applied Sensing Technology*, vol. 15, no. 9, pp. 56–74, 1998.

[13] S. Theobald, "High-Resolution Frequency Counter," *Electronics & Wireless World*, 1989.